Microwave-Field Sensing via Rydberg Entangling-Gate Dynamics

Y.-X. Song (宋宇炫),[1] C.-Z. Cao (曹传振),[1] G.-Q. Qin (秦国卿),[2,*] J.-Z. Han (韩济泽),[3,†] and M. Xue (薛明)[1,4,‡]

[1]*Department of Physics, Nanjing University of Aeronautics and Astronautics, Nanjing 211106, China.*
[2]*Beijing Institute of Radio Measurement Beijing, Beijing 100854, China.*
[3]*China Mobile (Suzhou) Software Technology Co., Ltd., Suzhou 215163, China.*
[4]*Key Laboratory of Aerospace Information Materials and Physics (NUAA), MIIT, Nanjing 211106, China*

(Dated: August 10, 2026)

Microwave-induced couplings to nearby Rydberg levels are usually regarded as a source of gate imperfections in neutral-atom quantum processors. Here we show that the same mechanism can instead be exploited as a metrological resource for microwave electrometry. We consider a laser-driven Rydberg controlled-Z gate subjected to an additional microwave coupling during the gate operation. The microwave field modifies the gate dynamics through coherent population leakage into an auxiliary Rydberg state, imprinting its amplitude and detuning onto the final two-qubit state. We characterize this response through the output-state fidelity, quantum Fisher information, and classical Fisher information. The results reveal parameter regimes in which enhanced sensitivity of the gate dynamics to microwave perturbations gives rise to increased estimation precision. Representative Rb and Cs implementations are used to illustrate the generality of the approach and to provide concrete sensitivity estimates. More broadly, our results demonstrate that calibrated quantum-gate dynamics can serve as a metrological resource, suggesting a gate-based sensing paradigm at the interface between quantum information processing and quantum sensing.

PACS numbers: 32.80.Ee, 07.07.Df, 06.20.Dk, 03.67.-a
Keywords: Rydberg atoms; microwave electrometry; quantum sensing; Fisher information

I. INTRODUCTION

Neutral-atom arrays have emerged as a leading platform for quantum information processing owing to their scalability, long coherence times, and programmable interactions enabled by highly excited Rydberg states [1–12]. A key capability of these systems is the realization of high-fidelity two-qubit entangling gates through the Rydberg blockade mechanism [13–22]. Considerable effort has therefore been devoted to suppressing decoherence, leakage, and unwanted couplings in order to improve gate fidelity and ultimately enhance the performance of large-scale neutral-atom quantum processors [23–27].

The same properties that make Rydberg atoms attractive for quantum information processing also make them highly sensitive probes of electromagnetic fields. Their large electric dipole moments enable strong interactions with microwave radiation and have motivated extensive studies of Rydberg electrometry based on spectroscopic shifts, Autler–Townes splitting, and electromagnetically induced transparency (EIT) [28–43]. In these approaches, the Rydberg atom primarily serves as a field-sensitive spectroscopic probe, and the sensing signal is extracted from changes in the atomic spectrum or optical response.

Quantum-information-processing platforms have recently attracted interest as metrological resources in addition to their computational applications [34, 44, 45]. In this context, microwave-induced couplings to nearby Rydberg levels are generally regarded as a source of gate imperfections in neutral-atom quantum processors, since they modify the intended gate dynamics, induce population leakage, and reduce the final gate fidelity [23, 25, 26, 46]. From a sensing perspective, however, the same susceptibility implies that the gate output carries information about the external microwave field. This observation raises a natural question: can the response of a Rydberg entangling gate to microwave perturbations be exploited as a metrological resource? If so, a calibrated quantum gate could simultaneously function as a sensing element, establishing a direct connection between gate errors and parameter estimation [47, 48]. Exploring this possibility offers a new route toward integrating quantum information processing and quantum sensing within a common physical platform [11].

In the present work, we consider a laser-driven Rydberg controlled-Z (CZ) gate subjected to an additional microwave field during the gate operation [23, 46]. The microwave field couples the gate Rydberg state to a nearby auxiliary Rydberg level, thereby perturbing the ideal gate dynamics. As a result, population can be transferred out of the intended excitation manifold, leading to a microwave-dependent modification of the final two-qubit state. Information about the microwave field is therefore encoded in the gate output and can be extracted through appropriate measurements.

To characterize this response, we analyze the gate fidelity together with the corresponding quantum Fisher information (QFI) and classical Fisher information (CFI). Using representative Rb and Cs implementations as illustrative examples [7, 8], we identify parameter regimes in which enhanced microwave sensitivity emerges from the same dynamical mechanisms responsible for gate imperfections. Our results demonstrate that calibrated entangling-gate dynamics can serve as a metrological resource for microwave electrometry, suggesting a gate-based sensing paradigm at the interface

* guoqing_qin@126.com
† hanjz16@tsinghua.org.cn
‡ mxue@nuaa.edu.cn

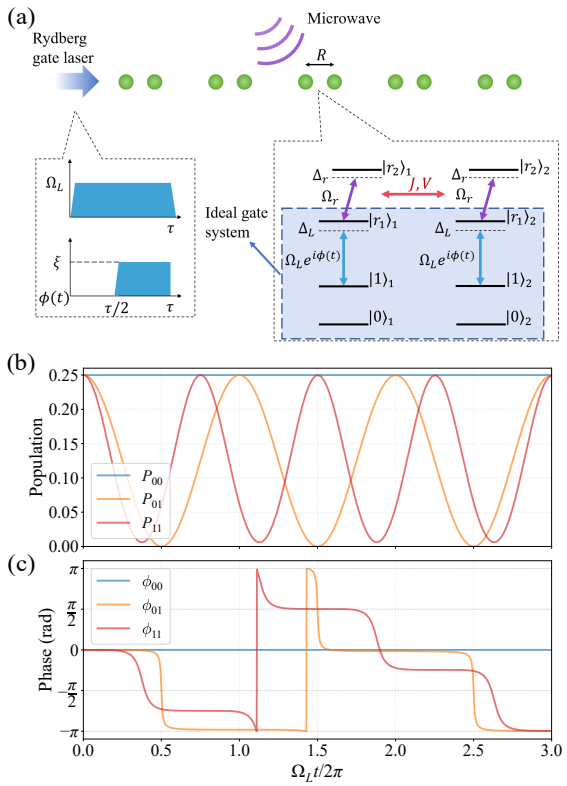


Figure 1. (a) Schematic illustration of the proposed gate-based microwave-sensing protocol. Two neutral atoms separated by a distance R are driven by laser fields that couple the computational state $|1\rangle$ to the Rydberg state $|r_1\rangle$. The CZ gate is implemented using a phase-modulated pulse sequence, in which the laser phase changes from 0 to ξ at $t = \tau/2$. An external microwave field couples $|r_1\rangle$ to a nearby Rydberg state $|r_2\rangle$ with Rabi frequency Ω_r and detuning Δ_r, providing a microwave-dependent modification of the gate dynamics. (b) Population and (c) phase evolution during the ideal CZ gate operation. Here $P_{ij} = |\langle ij|\psi(t)\rangle|^2$ denotes the population of the computational basis state $|ij\rangle$. The phases ϕ_{ij} denote the accumulated phases of the computational basis states $|ij\rangle$ relative to their initial values. Meanwhile, the states $|01\rangle$, $|10\rangle$, and $|11\rangle$ acquire a relative phase of π with respect to $|00\rangle$, resulting in the unitary operation $U_{\rm CZ} = \mathrm{diag}(1,-1,-1,-1)$.

between quantum information processing and quantum sensing.

II. PHYSICAL MODEL AND METHODS

A. Ideal Rydberg controlled-Z gate

As illustrated in Fig. 1(a), we consider neutral-atom qubits with computational states $|0\rangle$ and $|1\rangle$ and a Rydberg state $|r_1\rangle$. The CZ gate is implemented using the phase-modulated protocol introduced in Ref. [23]. The gate operation relies on the Rydberg blockade mechanism [14, 26], where strong interactions between simultaneously excited Rydberg atoms generate conditional excitation dynamics and state-dependent phase accumulation.

The gate dynamics are governed by

$$H_0 = \Delta_L \sum_{j=1,2} |r_1\rangle_j \langle r_1| + \frac{\Omega_L}{2} \sum_{j=1,2} (e^{i\phi(t)} |1\rangle_j \langle r_1| + H.c.) + V_{11} |r_1 r_1\rangle \langle r_1 r_1| . \quad (1)$$

where Ω_L and Δ_L are the Rabi frequency and detuning of the laser drive, $\phi(t)$ is the time-dependent laser phase shown in Fig. 1(a), and V_{11} denotes the interaction-induced energy shift of the doubly excited Rydberg state $|r_1 r_1\rangle$.

The population and phase evolution of the computational basis states are shown in Fig. 1(b) and (c). The states $|01\rangle$ and $|10\rangle$ undergo closed excitation cycles involving the singly excited Rydberg manifold, while $|11\rangle$ evolves through the blockade-coupled state $|W\rangle = (|1r_1\rangle + |r_1 1\rangle)/\sqrt{2}$ with transient occupation of $|r_1 r_1\rangle$. At the end of the pulse sequence, all population returns to the computational subspace, whereas different computational basis states acquire distinct dynamical phases, thereby realizing the CZ gate operation. The resulting operation in the computational basis $\{|00\rangle, |01\rangle, |10\rangle, |11\rangle\}$ is

$$U_{\rm CZ} = \mathrm{diag}(1,-1,-1,-1).$$

This operation is locally equivalent to the conventional controlled-Z gate, $\mathrm{diag}(1,1,1,-1)$, up to single-qubit Z phases.

B. Microwave-coupled Rydberg dynamics

To describe the response of the gate to an external microwave field, we extend the Hilbert space by introducing an auxiliary Rydberg state $|r_2\rangle$ in addition to the gate Rydberg state $|r_1\rangle$. The total Hamiltonian can be written as

$$H = H_0 + H_{\rm mw}, \quad (2)$$

where H_0 describes the ideal CZ gate dynamics and

$$H_{\rm mw} = H_{\rm drive} + H_{\rm ex} + H_{\rm int} \quad (3)$$

contains the microwave-induced contributions [46].

The microwave drive coupling the states $|r_1\rangle$ and $|r_2\rangle$ is

$$H_{\rm drive} = \Delta_r \sum_{j=1,2} |r_2\rangle_j \langle r_2| + \frac{\Omega_r}{2} \sum_{j=1,2} \left(|r_1\rangle_j \langle r_2| + \mathrm{H.c.} \right), \quad (4)$$

where Ω_r and Δ_r denote the microwave Rabi frequency and detuning, respectively. The resonant dipole-exchange interaction between the two atoms is

$$H_{\rm ex} = J \left(|r_1 r_2\rangle \langle r_2 r_1| + \mathrm{H.c.} \right), \quad (5)$$

with J the exchange coupling strength. Finally, the state-dependent Rydberg interactions beyond the ideal $|r_1 r_1\rangle$ blockade term are described by

$$H_{\rm int} = \sum\nolimits'_{m,n} V_{mn} |r_m r_n\rangle \langle r_m r_n| , \quad (6)$$

where V_{mn} is the interaction energy associated with the Rydberg pair state $|r_m r_n\rangle$ [49]. The prime indicates exclusion of the $(m,n)=(1,1)$ term, which is already included in H_0.

To quantify the influence of microwave-induced perturbations on the gate dynamics, we compare the final state generated by the perturbed evolution with the ideal CZ gate output. Starting from the input state

$$|\psi_0\rangle = |+\rangle \otimes |+\rangle\,, \qquad |+\rangle = \frac{1}{\sqrt{2}}(|0\rangle + |1\rangle). \tag{7}$$

the ideal gate output is $|\psi_{\rm id}\rangle = U_{\rm CZ}\,|\psi_0\rangle$. We characterize the gate response through the output-state fidelity

$$\mathcal{F} = \langle\psi_{\rm id}|\,\rho_{\rm out}\,|\psi_{\rm id}\rangle = \langle\psi_0|\,U_{\rm CZ}^{\dagger}\rho_{\rm out}U_{\rm CZ}\,|\psi_0\rangle\,, \tag{8}$$

where $\rho_{\rm out}$ denotes the density matrix at the completion of the gate sequence [50–52]. This quantity measures the overlap between the actual output state and the ideal CZ gate output $|\psi_{\rm id}\rangle$, and therefore provides a convenient measure of the susceptibility of the gate dynamics to microwave-induced perturbations.

To account for the finite lifetimes of the Rydberg states, we describe the system dynamics using a Lindblad master equation. For each atom, we introduce an auxiliary dump state $|d\rangle$ that collects population lost from the Rydberg states $|r_1\rangle$ and $|r_2\rangle$. This dump-state model provides a phenomenological description of spontaneous decay without explicitly resolving the detailed decay channels of the Rydberg manifold [46, 50, 51]. The density matrix evolves according to

$$\frac{d\rho}{dt} = -i[H,\rho] + \sum_{j=1}^{2}\sum_{m=1}^{2}\mathcal{D}[L_{j,m}]\,\rho, \tag{9}$$

where the Lindblad dissipator is defined as

$$\mathcal{D}[L]\rho = L\rho L^{\dagger} - \frac{1}{2}\left(L^{\dagger}L\rho + \rho L^{\dagger}L\right), \tag{10}$$

with jump operators $L_{j,m} = \sqrt{\Gamma_m}\,|d\rangle_j\,\langle r_m|$. Here Γ_m denotes the decay rate of the Rydberg state $|r_m\rangle$.

C. Fisher information

The output state after the gate evolution is denoted by $\rho_{\rm out}(\Omega_r,\Delta_r)$. To characterize the microwave sensitivity of the gate dynamics, we evaluate the quantum and classical Fisher information with respect to the microwave Rabi frequency Ω_r, with Δ_r treated as a fixed control parameter.

The quantum Fisher information (QFI) with respect to θ is defined as [48, 53]

$$F_Q(\theta) = \mathrm{Tr}[\rho_{\rm out}(\theta)L_\theta^2], \tag{11}$$

where L_θ is the symmetric logarithmic derivative (SLD) determined by

$$\partial_\theta\rho_{\rm out}(\theta) = \frac{1}{2}\left[L_\theta\rho_{\rm out}(\theta) + \rho_{\rm out}(\theta)L_\theta\right]. \tag{12}$$

Writing the density matrix in its eigenbasis as $\rho_{\rm out}(\theta) = \sum_i \lambda_i\,|i\rangle\,\langle i|$, the matrix elements of the SLD equation are

$$\langle i|\,\partial_\theta\rho_{\rm out}(\theta)\,|j\rangle = \frac{\lambda_i+\lambda_j}{2}\,\langle i|\,L_\theta\,|j\rangle\,. \tag{13}$$

Therefore,

$$\langle i|\,L_\theta\,|j\rangle = \frac{2\,\langle i|\,\partial_\theta\rho_{\rm out}(\theta)\,|j\rangle}{\lambda_i+\lambda_j}, \qquad \lambda_i+\lambda_j \neq 0. \tag{14}$$

Substituting these matrix elements into the definition of F_Q and symmetrizing the summation over i and j gives the expression below

$$F_Q(\theta) = \sum_{i,j}\frac{2}{\lambda_i+\lambda_j}\,|\langle i|\partial_\theta\rho_{\rm out}(\theta)|j\rangle|^2\,, \tag{15}$$

where λ_i and $|i\rangle$ denote the eigenvalues and eigenvectors of $\rho_{\rm out}(\theta)$. The QFI gives the maximum sensitivity allowed by quantum mechanics and sets the quantum Cramér–Rao bound (QCRB)

$$\Delta\theta \geq \frac{1}{\sqrt{\nu F_Q(\theta)}}, \tag{16}$$

where ν is the number of independent repetitions [48]. A larger QFI therefore indicates that the output states generated by slightly different microwave Rabi frequencies are more distinguishable in principle.

The QFI gives the maximum Fisher information attainable by optimizing over all measurements on the output state. To evaluate the information accessible from a specified measurement, we also calculate the classical Fisher information (CFI). For a measurement with outcome probabilities $p_k(\theta)$, the CFI is

$$F_C(\theta) = \sum_k \frac{1}{p_k(\theta)}\left[\frac{\partial p_k(\theta)}{\partial\theta}\right]^2, \tag{17}$$

where terms with $p_k(\theta)=0$ are omitted. The corresponding Cramér–Rao bound is

$$\Delta\theta \geq \frac{1}{\sqrt{\nu F_C(\theta)}}. \tag{18}$$

In the results below, we evaluate both F_Q and F_C for estimating Ω_r across the (Ω_r,Δ_r) parameter space. The QFI provides the ultimate precision bound, while the CFI characterizes the performance of the chosen measurement scheme. The Fisher-information analysis is local in parameter space. We therefore interpret the protocol as estimating a small variation $\delta\Omega_r$ around a calibrated operating point $\Omega_{r,0}$,

$$\Omega_r = \Omega_{r,0} + \delta\Omega_r. \tag{19}$$

The detuning Δ_r is treated as a calibrated control parameter.

Parameter	Rb ($n = 60$)	Cs ($n = 70$)
R (μm)	3.98	4.84
J (MHz)	$(2\pi)\,70$	$(2\pi)\,70$
$V_{11}/J, V_{22}/J$	0.037, 0.496	-0.086, 0.720
V_{12}/J	0.107	0.121
Γ_1^{-1}, Γ_2^{-1} (μs)	423, 252	913, 372
Ω_L (MHz)	$(2\pi)\,1.656$	$(2\pi)\,3.852$
Δ_L (MHz)	$(2\pi)\,-0.032$	$(2\pi)\,0.075$
ξ	$(2\pi)\,0.028$	$(2\pi)\,-0.028$
τ (μs)	1.81	0.78

Table I. Parameters used in the numerical simulations for the representative ^{87}Rb and ^{133}Cs implementations, including the exchange coupling strength J, Rydberg lifetimes $\Gamma_{1,2}^{-1}$, and optimized CZ gate parameters. The interaction is symmetric under particle exchange, such that $V_{12} = V_{21}$.

The Rydberg levels are chosen as $|r_1\rangle = |nP_{3/2}, m_J = 3/2\rangle$ and $|r_2\rangle = |nS_{1/2}, m_J = 1/2\rangle$.

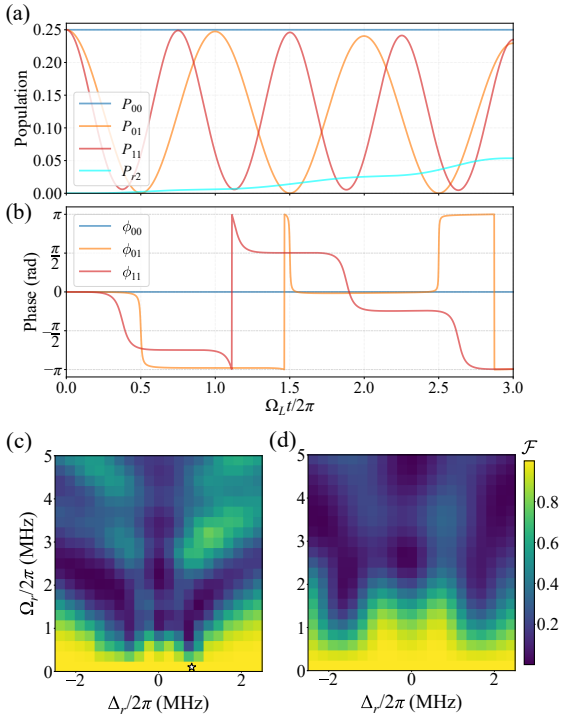


Figure 2. Microwave-induced leakage and fidelity response of the Rydberg CZ gate. (a) Population evolution and (b) phase evolution for the Rb implementation at the Rabi frequency $\Omega_r = 2\pi \times 0.1$ MHz and detuning $\Delta_r = 2\pi \times 0.8$ MHz. Here P_{r_2} denotes the total population in states involving $|r_2\rangle$. The microwave coupling induces a finite population leakage to $|r_2\rangle$, while leaving the accumulated computational-state phases nearly unaffected. (c) and (d) Output-state fidelity $\mathcal{F}$ as a function of Ω_r and Δ_r for the Rb and Cs implementations, respectively. The star in (c) marks the microwave parameters used in (a) and (b). Regions of rapid fidelity variation indicate enhanced sensitivity of the gate dynamics to microwave perturbations.

III. MICROWAVE-INDUCED EFFECTS ON GATE DYNAMICS AND SENSITIVITY

We now investigate the response of the Rydberg CZ gate in the presence of an additional microwave field. Two implementations based on Rb and Cs atoms are considered here. The two implementations have the same exchange coupling strength $J = (2\pi)\ 70$ MHz, allowing a direct comparison of their gate dynamics and sensing performance [46]. Relevant simulation parameters are summarized in Table I. The gate parameters Ω_L, Δ_L, ξ, and τ were optimized separately for the Rb and Cs implementations by maximizing the microwave-free output-state fidelity,

$$\{\Omega_L, \Delta_L, \xi, \tau\}_{\text{opt}} = \underset{\Omega_L, \Delta_L, \xi, \tau}{\arg\max}\ \mathcal{F}(\Omega_r = 0), \qquad (20)$$

subject to the constraint $\Omega_L \tau/(2\pi) = 3$.

For both implementations, the Rydberg lifetimes $\Gamma_{1,2}^{-1}$ are much longer than the gate duration, ensuring CZ gate fidelities above 0.997 in the absence of microwave perturbations. In the following subsections, the gate parameters are fixed at their values optimized for the microwave-free case, while the microwave parameters (Ω_r, Δ_r) are varied to characterize the response.

A. Microwave-perturbed gate dynamics

We first investigate how a microwave field modifies the CZ gate dynamics. During the gate operation, the coupling between $|r_1\rangle$ and $|r_2\rangle$ introduces an additional excitation pathway beyond the ideal gate manifold, perturbing the closed population trajectories required for high-fidelity gate operation. Fig. 2(a) and (b) show population and phase evolution for the Rb implementation. Compared with the ideal gate dynamics shown in Fig. 1(b), the dominant effect of the microwave field is population transfer from the gate state $|r_1\rangle$ to the auxiliary state $|r_2\rangle$. As a result, a finite population remains outside the ideal gate manifold at the end of the pulse sequence. In contrast, the accumulated phases of the computational states are only weakly modified. The microwave perturbation therefore manifests primarily as coherent leakage into the auxiliary state. These results indicate that the microwave sensitivity arises primarily from transient Rydberg-state population and the resulting microwave-induced leakage, while entanglement does not play a primary role in the present sensing mechanism.

The leakage dynamics directly affect the gate output. Fig. 2(c) and (d) show the corresponding output-state fidelity $\mathcal{F}$ as a function of the Rabi frequency Ω_r and detuning Δ_r for the Rb and Cs implementations, respectively. In the weak-coupling regime $\Omega_r \approx 0$, the evolution remains close to the ideal CZ gate trajectory and the fidelity stays near unity. As Ω_r increases, stronger leakage into $|r_2\rangle$ leads to larger reduction of the fidelity. The fidelity response exhibits a pronounced dependence on the detuning Δ_r. For the Rb implementation, the largest reduction occurs near $|\Delta_r| \approx (2\pi)\ 0.8$ MHz, and $|\Delta_r| \approx (2\pi)\ 1.8$ MHz for the Cs implementation. In these regimes, small variations of Ω_r produce

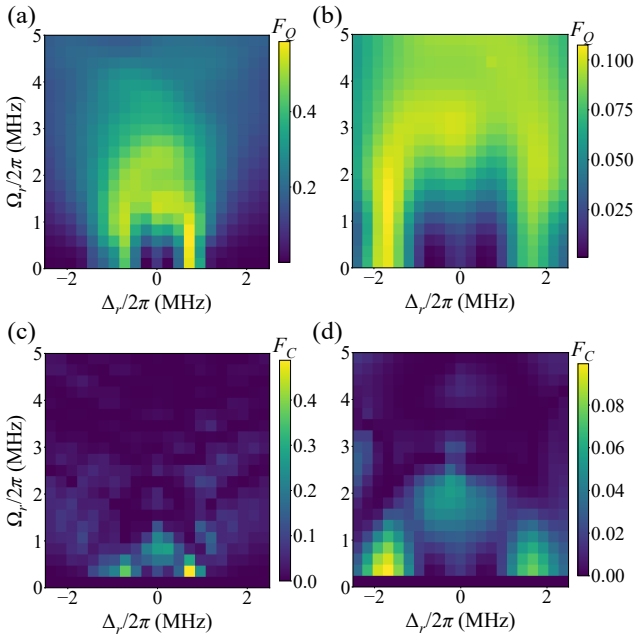


Figure 3. QFI F_Q and CFI F_C for estimating the Rabi frequency Ω_r, shown as functions of Ω_r and detuning Δ_r. (a) and (b) QFI for the Rb and Cs implementations, respectively. (c) and (d) CFI for the Rb and Cs implementations, respectively, obtained from the BPM. Accordingly, F_Q and F_C are given in units of μs^2.

large changes in the gate output, indicating enhanced susceptibility of the gate dynamics to the microwave field. This strong parameter dependence suggests that the gate dynamics may serve as a sensitive probe of Ω_r.

B. Quantum and classical sensitivity landscapes

To quantify the sensitivity of the microwave-perturbed gate dynamics, we evaluate both the QFI and the CFI for estimating the Rabi frequency Ω_r. Fig. 3 shows the QFI and CFI landscapes for the Rb and Cs implementations. For both atomic implementations, the Fisher information exhibits localized regions of pronounced enhancement. These regions coincide with the steepest variations in gate fidelity, indicating that the output state is highly susceptible to small variations of Ω_r. As discussed in the previous subsection, the microwave field induces coherent leakage from the gate state $|r_1\rangle$ into the auxiliary state $|r_2\rangle$. Near the sensitive points, such as the marked point in Fig. 2(c), this leakage changes rapidly with Ω_r, producing large variations in the final state and consequently enhancing both the QFI and CFI.

Although the sensitivity distributions are qualitatively similar, quantitative differences remain between the two atomic implementations. The Rb implementation exhibits larger peak Fisher information, and the Cs implementation exhibits broader high-sensitivity regions. This difference can be attributed to the shorter gate duration of the Cs implementation, which reduces the accumulation of microwave-induced perturbations during the evolution.

The QFI sets the ultimate sensitivity allowed by quantum mechanics, but the achievable sensitivity depends on the specific measurement strategy. We therefore evaluate the CFI for experimentally accessible measurements. The fidelity defined in Eq. (8) naturally provides a binary projective measurement (BPM) onto the ideal output state $|\psi_{\rm id}\rangle$, with the measurement operators

$$\Pi_0 = |\psi_{\rm id}\rangle\langle\psi_{\rm id}|, \qquad \Pi_1 = I - \Pi_0. \tag{21}$$

The corresponding outcome probabilities are

$$p_0(\Omega_r) = \mathrm{Tr}[\Pi_0\rho(\Omega_r)]\,, \qquad p_1(\Omega_r) = 1 - p_0(\Omega_r), \tag{22}$$

note that $p_0(\Omega_r)$ is exactly equal to $\mathcal{F}$. The BPM may be implemented by applying a calibrated CZ gate followed by Hadamard rotations on both qubits, which maps $|\psi_{\rm id}\rangle$ onto $|00\rangle$, followed by state-resolved fluorescence detection. The CFI is calculated directly from the binary probability distribution $\{p_0, p_1\}$ via Eq. (17). Fig. 3(c) and (d) show the CFI for two atomic implementations. Similar to the QFI, the CFI exhibits pronounced enhancement within localized regions.

To further investigate the information that can be extracted from the output state, we next consider Bell-basis measurements (BBM). In this case, the final state is projected onto the Bell states $|B_k\rangle \in \{|\Phi^+\rangle, |\Phi^-\rangle, |\Psi^+\rangle, |\Psi^-\rangle\}$, where $|\Phi^\pm\rangle = \frac{1}{\sqrt{2}}(|00\rangle \pm |11\rangle)$ and $|\Psi^\pm\rangle = \frac{1}{\sqrt{2}}(|01\rangle \pm |10\rangle)$. The corresponding Bell-state probabilities are

$$p_k(\Omega_r) = \langle B_k|\rho(\Omega_r)|B_k\rangle, \tag{23}$$

where $k \in \{\Phi^+, \Phi^-, \Psi^+, \Psi^-\}$. Since the population leakage may prevent the system from returning to the computational subspace at the end of the gate evolution, we additionally define the leakage probability

$$p_{\rm leak}(\Omega_r) = 1 - \sum_k p_k(\Omega_r). \tag{24}$$

A Bell-basis measurement can be implemented using an additional entangling operation and single-qubit rotations before computational-basis readout [54]. Population outside the computational subspace is grouped into the leakage outcome. The CFI is then calculated from the five-outcome probability distribution

$$\{p_{\Phi^+}, p_{\Phi^-}, p_{\Psi^+}, p_{\Psi^-}, p_{\rm leak}\}\,. \tag{25}$$

As shown in Fig. 4, the CFI obtained from both the BPM and BBM approaches the corresponding QFI in parts of the weak-coupling regimes. This indicates that the simple projective measurement considered here approaches optimal performance in certain parameter regions, capturing most of the information in the state.

Finite detection errors may be modeled by a classical confusion matrix acting on the ideal outcome probabilities. Such errors generally reduce the accessible CFI by decreasing the distinguishability between neighboring probability distributions, while their quantitative impact depends on the specific experimental readout scheme. [55, 56]

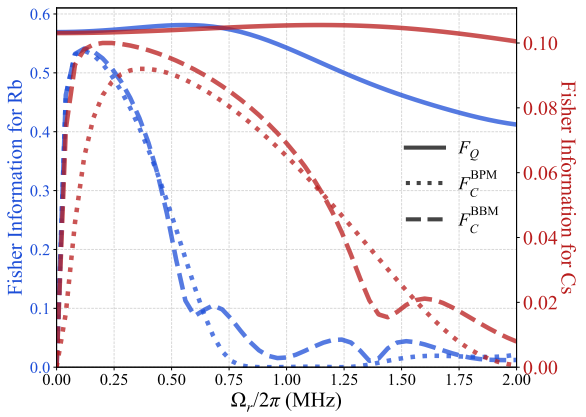


Figure 4. Comparison of the QFI F_Q (solid lines) and the CFI obtained from the BPM, F_C^{BPM} (dotted lines) and the BBM, (dashed lines) F_C^{BBM}, evaluated along representative high-sensitivity cuts. Blue curves correspond to the Rb implementation at $\Delta_r = 2\pi \times 0.8$ MHz, red curves correspond to the Cs implementation at $\Delta_r = -2\pi \times 1.8$ MHz.

The achievable uncertainty for estimating the Rabi frequency Ω_r is $\Delta\Omega_r = 1/\sqrt{\nu F_C(\Omega_r)}$, as given in Eq. (18). For the single-shot case ($\nu = 1$), the maximum CFI, obtained at the optimal parameters (Ω_r, Δ_r), yields $\Delta\Omega_r/(2\pi) = 0.23$ MHz for Rb and 0.50 MHz for Cs.

The microwave electric field amplitude E_{MW} is determined from the measured Rabi frequency Ω_r via the relation $\Omega_r/E_{\mathrm{MW}} = d/\hbar$, where d is the transition dipole moment between the Rydberg states, and $\hbar$ is the reduced Planck constant [34]. Here, E_{MW} denotes the effective microwave electric-field amplitude associated with the selected $|r_1\rangle \leftrightarrow |r_2\rangle$ transition, and the quoted transition dipole matrix element is used in converting Ω_r into the corresponding field amplitude.

Using the dipole transition matrix elements of the relevant Rydberg states [49], we obtain $\Omega_r/E_{\mathrm{MW}} = 2\pi \times 2721\ \mathrm{MHz}/(\mathrm{V\,cm^{-1}})$ for Rb and $\Omega_r/E_{\mathrm{MW}} = 2\pi \times 2632\ \mathrm{MHz}/(\mathrm{V\,cm^{-1}})$ for Cs.

The corresponding microwave-field uncertainty is therefore

$$\Delta E_{\mathrm{MW}} = \frac{\Delta\Omega_r}{\Omega_r/E_{\mathrm{MW}}}. \tag{26}$$

Substituting the optimal values obtained above gives

$$\Delta E_{\mathrm{MW}} = 8.4 \times 10^{-5}\ \mathrm{V\,cm^{-1}}$$

for Rb and

$$\Delta E_{\mathrm{MW}} = 1.9 \times 10^{-4}\ \mathrm{V\,cm^{-1}}$$

for Cs. To characterize the intrinsic sensitivity associated with the coherent gate dynamics, we define the idealized sensitivity as

$$\eta_E = \Delta E_{\mathrm{MW}} \sqrt{\tau}, \tag{27}$$

where τ is the gate duration [47]. Using the gate durations for the two implementations, we obtain $\eta_E^{\mathrm{Rb}} \approx 1.1 \times 10^{-7}\ \mathrm{V\,cm^{-1}\,Hz^{-1/2}}$ and $\eta_E^{\mathrm{Cs}} \approx 1.7 \times 10^{-7}\ \mathrm{V\,cm^{-1}\,Hz^{-1/2}}$.

These idealized sensitivities are within approximately one order of magnitude of the best sensitivities reported for microwave electrometry using an array of independent Rydberg-atom sensors [34]. Since the present work employs a single CZ gate that was originally designed for quantum information processing rather than sensing, the reported values should not be regarded as the ultimate performance achievable within a gate-based sensing protocol. Further optimization of the gate-based sensing protocol may enable substantially enhanced sensitivity.

IV. DISCUSSION AND CONCLUSION

We propose a protocol for microwave field sensing using a Rydberg CZ gate. By analyzing the gate dynamics under microwave perturbation, we identify parameter regimes in which the gate output is strongly modified, thereby enhancing both the QFI and CFI. For both Rb and Cs implementations, the resulting idealized sensitivities reach the $10^{-7}\ \mathrm{V\,cm^{-1}\,Hz^{-1/2}}$ level, demonstrating the feasibility of exploiting neutral-atom entangling gates for microwave sensing.

Overall, these results demonstrate that calibrated gate dynamics can serve as a sensitive probe of microwave fields. More broadly, they illustrate how coherent quantum operations can be repurposed as metrological resources, providing a natural interface between quantum information processing and quantum sensing. While the present work focuses on a specific CZ gate protocol, the underlying idea is general and may be extended to other gate architectures and quantum computing platforms, opening new opportunities for integrating quantum control and quantum metrology within a common framework [11].

Acknowledgement— This work was supported by the National Natural Science Foundation of China (No. 12304543). Y.-X. S. acknowledges support from the Innovation Training Program of NUAA (No. 20251028700793X and No. 202610287102Z). J.-Z. H. acknowledges support from the Natural Science Foundation of Jiangsu Province (No. BK20250404), and the Youth Science and Technology Talent Support Project of Jiangsu Province (No. JSTJ-2025-600) and Suzhou (No. (2025)062). C.-Z. C. was supported by the Postgraduate Research & Practice Innovation Program of NUAA (No. xcxjh20252107). M.X. was supported by NUAA (No. 1018-ILF26028)

[1] Henriet L, Beguin L, Signoles A, Lahaye T, Browaeys A, Reymond G O and Jurczak C 2020 Quantum **4** 327

[2] Morgado M and Whitlock S 2021 AVS Quantum Sci. **3** 023501

[3] Picken C J, Legaie R, McDonnell K and Pritchard J D 2018 Quantum Science and Technology **4** 015011 ISSN 2058-9565
[4] Browaeys A and Lahaye T 2020 Nat. Phys. **16** 132–142
[5] Shi X F 2022 Quantum Science and Technology **7** 023002 ISSN 2058-9565
[6] Bluvstein D, Geim A A, Li S H, Evered S J, Bonilla Ataides J P, Baranes G, Gu A, Manovitz T, Xu M, Kalinowski M, Majidy S, Kokail C, Maskara N, Trapp E C, Stewart L M, Hollerith S, Zhou H, Gullans M J, Yelin S F, Greiner M, Vuletić V, Cain M and Lukin M D 2026 Nature **649** 39–46 ISSN 0028-0836, 1476-4687
[7] Bluvstein D, Levine H, Semeghini G, Wang T T, Ebadi S, Kalinowski M, Keesling A, Maskara N, Pichler H, Greiner M, Vuletić V and Lukin M D 2022 Nature **604** 451–456 ISSN 0028-0836, 1476-4687
[8] Graham T M, Song Y, Scott J, Poole C, Phuttitarn L, Jooya K, Eichler P, Jiang X, Marra A, Grinkemeyer B, Kwon M, Ebert M, Cherek J, Lichtman M T, Gillette M, Gilbert J, Bowman D, Ballance T, Campbell C, Dahl E D, Crawford O, Blunt N S, Rogers B, Noel T and Saffman M 2022 Nature **604** 457–462 ISSN 0028-0836, 1476-4687
[9] Wintersperger K, Dommert F, Ehmer T, Hoursanov A, Klepsch J, Mauerer W, Reuber G, Strohm T, Yin M and Luber S 2023 EPJ Quantum Technology **10** 32 ISSN 2662-4400, 2196-0763
[10] Sun C F, Chen X Y, Mu W L, Wang G C, You J B and Shao X Q 2024 EPJ Quantum Technology **11** 34 ISSN 2662-4400, 2196-0763
[11] Shen H and Zhang J 2025 National Science Review **12** nwaf149 ISSN 2095-5138, 2053-714X
[12] Manetsch H J, Nomura G, Bataille E, Lv X, Leung K H and Endres M 2025 Nature **647** 60–67 ISSN 0028-0836, 1476-4687
[13] Vogt T, Viteau M, Chotia A, Zhao J, Comparat D and Pillet P 2007 Physical Review Letters **99** 073002 ISSN 0031-9007, 1079-7114
[14] Jaksch D, Cirac J I, Zoller P, Rolston S L, Côté R and Lukin M D 2000 Phys. Rev. Lett. **85** 2208–2211
[15] Isenhower L, Urban E, Zhang X L, Gill A T, Henage T, Johnson T A, Walker T G and Saffman M 2010 Phys. Rev. Lett. **104**(1) 010503 URL https://link.aps.org/doi/10.1103/PhysRevLett.104.010503
[16] Wilk T, Gaëtan A, Evellin C, Wolters J, Miroshnychenko Y, Grangier P and Browaeys A 2010 Phys. Rev. Lett. **104**(1) 010502 URL https://link.aps.org/doi/10.1103/PhysRevLett.104.010502
[17] Graham T M, Kwon M, Grinkemeyer B, Marra Z, Jiang X, Lichtman M T, Sun Y, Ebert M and Saffman M 2019 Phys. Rev. Lett. **123** 230501
[18] Madjarov I S, Covey J P, Shaw A L, Choi J, Kale A, Cooper A, Pichler H, Schkolnik V, Williams J R and Endres M 2020 Nat. Phys. **16** 857–861
[19] Levine H, Keesling A, Omran A, Bernien H, Schwartz S, Zibrov A S, Endres M, Greiner M, Vuletić V and Lukin M D 2018 Phys. Rev. Lett. **121**(12) 123603 URL https://link.aps.org/doi/10.1103/PhysRevLett.121.123603
[20] Shi X F and Lu Y 2021 Phys. Rev. A **104**(1) 012615 URL https://link.aps.org/doi/10.1103/PhysRevA.104.012615
[21] Ma S, Burgers A P, Liu G, Wilson J, Zhang B and Thompson J D 2022 Phys. Rev. X **12**(2) 021028 URL https://link.aps.org/doi/10.1103/PhysRevX.12.021028
[22] Kurdak D, Banner P R, Li Y, Muleady S R, Gorshkov A V, Rolston S L and Porto J V 2025 Phys. Rev. Lett. **134**(12) 123404 URL https://link.aps.org/doi/10.1103/PhysRevLett.134.123404
[23] Levine H, Keesling A, Semeghini G, Omran A, Wang T T, Ebadi S, Bernien H, Greiner M, Vuletić V, Pichler H and Lukin M D 2019 Phys. Rev. Lett. **123** 170503
[24] Ma S, Liu G, Peng P, Zhang B, Jandura S, Claes J, Burgers A P, Pupillo G, Puri S and Thompson J D 2023 Nature **622** 279–284 ISSN 0028-0836, 1476-4687
[25] Evered S J, Bluvstein D, Kalinowski M, Ebadi S, Manovitz T, Zhou H, Li S H, Geim A A, Wang T T, Maskara N, Levine H, Semeghini G, Greiner M, Vuletić V and Lukin M D 2023 Nature **622** 268–272 ISSN 0028-0836, 1476-4687
[26] Saffman M, Walker T G and Mølmer K 2010 Rev. Mod. Phys. **82** 2313–2363
[27] Covey J P, Weinfurter H and Bernien H 2023 npj Quantum Information **9** 90
[28] Sedlacek J A, Schwettmann A, Kübler H, Löw R, Pfau T and Shaffer J P 2012 Nat. Phys. **8** 819–824
[29] Holloway C L, Gordon J A, Schwarzkopf A, Anderson D A, Miller S A, Thaicharoen N and Raithel G 2014 Appl. Phys. Lett. **104** 244102
[30] Anderson D A and Raithel G 2017 Appl. Phys. Lett. **111** 053504
[31] Jing M, Hu Y, Ma J, Zhang H, Zhang L, Xiao L and Jia S 2020 Nat. Phys. **16** 911–915
[32] Ding D S, Liu Z K, Shi B S, Guo G C, Mølmer K and Adams C S 2022 Nature Physics **18** 1447–1452 ISSN 1745-2473, 1745-2481
[33] Liu C R, Tao R, Lv X, Dong Y, Li C, Wei B and Zhou M 2026 Phys. Rev. Appl. **25**(3) 034052 URL https://link.aps.org/doi/10.1103/qsmd-yh44
[34] Zhang Y W, Xiang D S, Liao R, Liu H X, Xu B, Zhou P, Zhou Y, Zhang K and Li L 2026 Phys. Rev. Lett. **136**(11) 110802 URL https://link.aps.org/doi/10.1103/v5nm-xwp5
[35] Yuan J, Yang W, Jing M, Zhang H, Jiao Y, Li W, Zhang L, Xiao L and Jia S 2023 Reports on Progress in Physics **86** 106001 ISSN 0034-4885, 1361-6633
[36] Wu S, Zhang D, Li Z, Shi M, Yang P, Guo J, Du W, Bao G and Zhang W 2023 Phys. Rev. Appl. **20**(6) 064028 URL https://link.aps.org/doi/10.1103/PhysRevApplied.20.064028
[37] Zhang H, Ma Y, Liao K, Yang W, Liu Z, Ding D, Yan H, Li W and Zhang L 2024 Science Bulletin **69** 1515–1535 ISSN 20959273
[38] Cui Y, Jia F D, Hao J H, Wang Y H, Zhou F, Liu X B, Yu Y H, Mei J, Bai J H, Bao Y Y, Hu D, Wang Y, Liu Y, Zhang J, Xie F and Zhong Z P 2023 Phys. Rev. A **107**(4) 043102 URL https://link.aps.org/doi/10.1103/PhysRevA.107.043102
[39] Yang W, Jing M, Zhang H, Zhang L, Xiao L and Jia S 2023 Phys. Rev. Appl. **19**(6) 064021 URL https://link.aps.org/doi/10.1103/PhysRevApplied.19.064021
[40] Cai M, You S, Zhang S, Xu Z and Liu H 2023 Applied Physics Letters **122** 161103 ISSN 0003-6951, 1077-3118
[41] Yang B, Yan Y, Li X, Xiao L, Li X, Chen L, Deng J and Cheng H 2024 Phys. Rev. Appl. **21**(3) L031003 URL https://link.aps.org/doi/10.1103/PhysRevApplied.21.L031003
[42] Chen R, Wang D Y, Su S L and Li G X 2026 Phys. Rev. A **113**(4) 043724 URL https://link.aps.org/doi/10.1103/yw4q-t2fj
[43] Cai M, Wei A, Chen S and Huang Y 2025 Chinese Physics B **34** 083201 URL https://doi.org/10.1088/1674-1056/add005
[44] Aiache Y, El Allati A and El Anouz K 2024 Phys. Rev. A **110**(3)

032605 URL https://link.aps.org/doi/10.1103/PhysRevA.110.032605

[45] Bachain O, Jaloum E, Amazioug M, Altuijri R, Laamara R A, Sooppy Nisar K and Abdel-Aty A H 2026 Physics Letters A 131897 ISSN 03759601

[46] Giudici G, Veroni S, Giudice G, Pichler H and Zeiher J 2025 PRX Quantum **6**(3) 030308 URL https://link.aps.org/doi/10.1103/5d8p-3hm1

[47] Degen C L, Reinhard F and Cappellaro P 2017 Rev. Mod. Phys. **89**(3) 035002 URL https://link.aps.org/doi/10.1103/RevModPhys.89.035002

[48] Pezzè L, Smerzi A, Oberthaler M K, Schmied R and Treutlein P 2018 Rev. Mod. Phys. **90**(3) 035005 URL https://link.aps.org/doi/10.1103/RevModPhys.90.035005

[49] Šibalić N, Pritchard J, Adams C and Weatherill K 2017 Computer Physics Communications **220** 319–331 ISSN 00104655

[50] Pelegrí G, Daley A J and Pritchard J D 2022 Quantum Science and Technology **7** 045020 URL https://doi.org/10.1088/2058-9565/ac823a

[51] Xue M, Xu S, Li X and Li X 2024 Phys. Rev. A **110**(3) 032619 URL https://link.aps.org/doi/10.1103/PhysRevA.110.032619

[52] Hashim A, Nguyen L B, Goss N, Marinelli B, Naik R K, Chistolini T, Hines J, Marceaux J, Kim Y, Gokhale P, Tomesh T, Chen S, Jiang L, Ferracin S, Rudinger K, Proctor T, Young K C, Siddiqi I and Blume-Kohout R 2025 PRX Quantum **6**(3) 030202 URL https://link.aps.org/doi/10.1103/PRXQuantum.6.030202

[53] Braunstein S L and Caves C M 1994 Phys. Rev. Lett. **72**(22) 3439–3443 URL https://link.aps.org/doi/10.1103/PhysRevLett.72.3439

[54] Beckey J L, Pelegrí G, Foulds S and Pearson N J 2023 Phys. Rev. A **107**(6) 062425 URL https://link.aps.org/doi/10.1103/PhysRevA.107.062425

[55] Maciejewski F B, Zimborás Z and Oszmaniec M 2020 Quantum **4** 257 ISSN 2521-327X (*Preprint* 1907.08518)

[56] Kurdziałek S and Demkowicz-Dobrzański R 2023 Phys. Rev. Lett. **130**(16) 160802 URL https://link.aps.org/doi/10.1103/PhysRevLett.130.160802